Microfluid Nanofluid
DOI 10.1007/s10404-015-1619-8

RESEARCH PAPER

Bubbly flow and gas–liquid mass transfer in square and circular microchannels for stress-free and rigid interfaces: dissolution model

David Mikaelian[1] · Benoît Haut[1] · Benoit Scheid[1]

Received: 24 December 2014 / Accepted: 20 July 2015

Abstract A model is proposed to describe the dissolution of a chain of spherical pure gas bubbles into a non-volatile liquid, along square and circular microchannels. The gas–liquid interface is considered stress-free or rigid. This model enables predicting, in each considered case, the evolution along the microchannel of the bubble diameter, the bubble velocity, the separation distance between two successive bubbles, the liquid fraction, the pressure in both the liquid and the gas phases, the concentration of the dissolved gas in the liquid phase and the mass transfer coefficient between the bubble and the liquid phase. The influence on the gas dissolution of the interfacial boundary condition, the microchannel type, the operating conditions and the physicochemical properties of the liquid and gas is analyzed. Existing experimental data for a nearly square microchannel are convincingly reproduced using the model. The validity and the different applications of the model are also discussed.

Keywords Microfluidics · Absorption · Square microchannel · Circular microchannel · Bubbly flow · Spherical bubbles

1 Introduction

Nowadays, microfluidic devices are increasingly used for fundamental and exploratory studies in chemistry and biology. The main advantages are rapid heat and mass transfer, rigorous control of the operating conditions and small volumes, which are important for hazardous and expensive reagents. Two-phase microfluidics, in particular droplet-based microfluidics, has the additional advantage to avoid dispersion of residence times and thus enhances chemical and biochemical screening, protein crystallization, enzymatic kinetics and assays (Song et al. 2006). More recently, droplets have been replaced by bubbles to study gas–liquid physical processes in microfluidics (see, e.g., Kashid et al. 2011 and references therein). Carbon dioxide-related studies in so-called segmented-flow microfluidics have specifically been abundant over the past years (Abolhasani et al. 2014), including dissolution of CO_2 in solvents such as water (Sun and Cubaud 2011), CO_2 reaction and sequestration (Voicu et al. 2014) and the use of supercritical CO_2 as a "green" solvent (Leitner 2002). In that context, and given the importance of bubble–liquid mass transfer in these microfluidic applications, the present paper aims at modeling the dissolution of a chain of gas bubbles in microchannels.

Gas–liquid two-phase flow patterns in microchannels were investigated by Cubaud and Ho (2004) and by Kim et al. (2011) in square and rectangular microchannels, respectively. In both works, five regimes were reported, depending on the gas and liquid superficial velocities in the microchannel and named by Cubaud and Ho (2004) as the bubbly, the wedging, the slug, the annular and the dry flows. Similar regimes were observed in circular channels of 1 mm diameter by Triplett et al. (1999a, b).

Additionally, the presence of surface-active contaminants can have a great influence on the dynamics and morphology of a bubble in a microchannel, because they can modify the boundary conditions at the bubble–liquid interface (Haberman and Morton 1953; Clift et al. 1978). Indeed, surface

✉ David Mikaelian
dmikaeli@ulb.ac.be

[1] Transfers, Interfaces and Processes (TIPs), CP 165/67, Université libre de Bruxelles, Av. F. D. Roosevelt 50, 1050 Brussels, Belgium

Published online: 15 August 2015

concentration gradients of surfactant induced by the relative motion of the bubble into the liquid provoke surface stresses that usually "rigidify" the bubble surface and lead to a bubble behavior similar to a rigid body.

In this paper, we exclusively investigate the bubbly flow regime in square and circular microchannels. The bubbly flow corresponds to discrete spherical bubbles, with diameters smaller than the microchannel hydraulic diameter, moving in a continuous liquid phase. To the best of our knowledge, a mathematical model to describe the dissolution of a chain of bubbles into a liquid along a square or a circular microchannel, taking into account convective effects in the liquid, has not been proposed yet for the bubbly flow regime. In the work of Cubaud et al. (2012), a bubbly flow was observed when investigating experimentally the dissolution of CO_2 bubbles in water in a nearly square microchannel. Nevertheless, the mass transfer between these bubbles and the surrounding liquid was not quantified in this work. The dissolution of CO_2 bubbles in sodium dodecyl sulfate (SDS) solutions along a rectangular microchannel was investigated by Shim et al. (2014) and a dissolution model was proposed. However, the considered Péclet numbers allowed neglecting, in this model, convective effects on the gas–liquid mass transfer. Furthermore, only confined, i.e., non-spherical, bubbles were considered in that work.

In our previous work (Mikaelian et al. 2015), a numerical procedure was developed in order to analyze the dynamics of a spherical bubble among a chain of bubbles in a square or a circular microchannel, as well as the mass transfer between this bubble and the surrounding liquid. In that work, incompressible Newtonian liquids were considered, with homogeneous and time-independent viscosity and density. The bubble was assumed spherical and located at the center of the microchannels. A one-sided approach was adopted; i.e., assuming that the bubble–liquid mass transfer was limited by phenomena taking place in the liquid phase. Furthermore, in a reference frame attached to the bubble, the liquid flow and the mass transport in the liquid were considered quasi-steady; i.e., the time derivatives in the mass and momentum transport equations in the liquid phase were set to zero.

Two limiting cases were considered in our previous work (Mikaelian et al. 2015) regarding the gas–liquid interface: a stress-free interface (i.e., no viscous stress is exerted by the bubble on the liquid, such that a stress-free condition is applied at the interface) and a rigid interface (i.e., the bubble behaves as a solid sphere such that a no-slip condition is applied at the interface). Results obtained with the developed numerical procedure were used in order to establish correlations expressing the velocity of the bubble and the Sherwood number, characterizing the mass transfer between the bubble and the surrounding liquid, as functions of the control parameters of the system. These correlations are presented in Table 1 with notations defined in Table 2; they were obtained for a sufficiently large computational periodic domain (the length of which represents the distance between two successive bubbles), such that they are independent of its length.

This previous work (Mikaelian et al. 2015) focused on the scale of a single spherical bubble, at quasi-steady state in a microchannel. In the present paper, the correlations

Table 2 Notations and dimensionless numbers

Symbol	Description	Expression
V_B	Bubble velocity ($\mathrm{m\,s^{-1}}$)	$J_A = \frac{Q_L+Q_G}{A_\Sigma}$
Q_L	Liquid volumetric flow rate ($\mathrm{m^3\,s^{-1}}$)	
Q_G	Gas volumetric flow rate ($\mathrm{m^3\,s^{-1}}$)	
A_Σ	Area of the cross section of the microchannel ($\mathrm{m^2}$)	
J_A	Total superficial velocity ($\mathrm{m\,s^{-1}}$)	
d	Bubble diameter (m)	
d_h	Hydraulic diameter of the microchannel (m)	
D	Diffusion coefficient of the gas into the liquid ($\mathrm{m^2\,s^{-1}}$)	
ρ	Density of the liquid ($\mathrm{kg\,m^{-3}}$)	
μ	Dynamic viscosity of the liquid (Pa s)	
k_l	Bubble–liquid mass transfer coefficient ($\mathrm{m\,s^{-1}}$)	
Re	Reynolds number	$\mathrm{Re} = \frac{\rho V_B d}{\mu}$
Sc	Schmidt number	$\mathrm{Sc} = \frac{\mu}{\rho D}$
Sh	Sherwood number	$\mathrm{Sh} = \frac{k_l d}{D}$

Table 1 Correlations obtained in Mikaelian et al. (2015) for the different cases considered in that paper

	Square microchannel		Circular microchannel	
Stress-free interface	$\frac{V_B}{J_A} = 1 + 1.1\exp\left[-\left(\frac{d}{d_h}\right)^5\right]$	(1)	$\frac{V_B}{J_A} = 1 + \exp\left[-1.83\left(\frac{d}{d_h}\right)^5\right]$	(3)
	$\mathrm{Sh} = 2 + 3\,\mathrm{Re}^{1/3}\mathrm{Sc}^{1/3}\frac{d}{d_h}$	(2)	$\mathrm{Sh} = 2 + 2\,\mathrm{Re}^{2/5}\mathrm{Sc}^{2/5}\frac{d}{d_h}$	(4)
Rigid interface	$\frac{V_B}{J_A} = 1 + 1.1\exp\left[-1.5\left(\frac{d}{d_h}\right)^{9/4}\right]$	(5)	$\frac{V_B}{J_A} = 1 + \exp\left[-1.92\left(\frac{d}{d_h}\right)^{9/4}\right]$	(7)
	$\mathrm{Sh} = 2 + 1.6\,Re^{1/3}\mathrm{Sc}^{1/3}\frac{d}{d_h}$	(6)	$\mathrm{Sh} = 2 + 1.8\,Re^{1/3}\mathrm{Sc}^{1/3}\frac{d}{d_h}$	(8)

They were established for $0.15 \le d/d_h \le 0.75$, $1.70 \le \mathrm{Re} \le 39.84$ and $152 \le \mathrm{Sc} \le 551.3$

presented in Table 1 are integrated into a mathematical model of a whole microchannel, where a chain of spherical bubbles is dissolving into a liquid. This so-called dissolution model is based on mass and momentum balances. It is a continuous model in which variables, such as the liquid and gas pressures, the bubble diameter, the dissolved gas concentration, the distance between two successive bubbles, the bubble velocity, the liquid fraction and the mass transfer coefficient, are written as continuous functions of a coordinate along the microchannel. Pure gas bubbles are considered in this model, with either a stress-free or a rigid interface, in a square or a circular microchannel.

The dissolution model development is presented in Sect. 2. In Sect. 3, the model is used in order to demonstrate its capabilities and compare its solutions to experimental data available in the literature. In Sect. 4, different applications of the model as well as its validity are discussed. Conclusions and perspectives are presented in Sect. 5.

2 Dissolution model

We first define a coordinate x along the microchannel, with the origin placed at the position where spherical bubbles are generated, ensuring that the ranges for applying the correlations of Table 1 are respected. Unless specified otherwise, the notations used in the dissolution model are given in Table 2.

The liquid fraction $\alpha_L(x)$ is defined as

$$\alpha_L(x) = \frac{Q_L}{Q_L + Q_G(x)}, \tag{9}$$

where Q_L is taken independent of x thanks to the fact that the gas density is much lower than the liquid density, such that the amount of gas dissolved into the liquid does not significantly affect its flow rate. Denoting $\ell(x)$ the distance between the center of two successive bubbles, as depicted in Fig. 1, one can write $Q_G(x) = \frac{\pi d(x)^3}{6\ell(x)} V_B(x)$, and expressing the total superficial velocity as $J_A(x) = \frac{Q_L + Q_G(x)}{A_\Sigma}$, Eq. 9 can be rewritten as

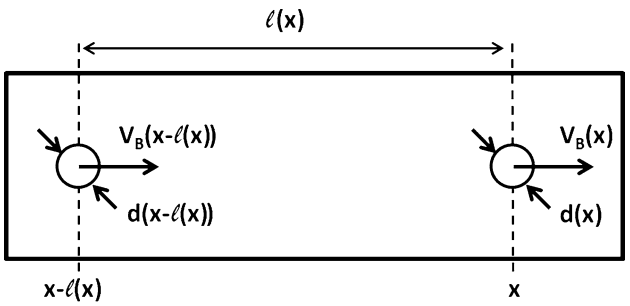

Fig. 1 Representation of two successive bubbles in the microchannel

$$\alpha_L(x) = 1 - \frac{\pi d(x)^3}{6A_\Sigma \ell(x)} \frac{V_B(x)}{J_A(x)}. \tag{10}$$

It can be shown (see "Separation distance between two successive bubbles along the microchannel" section of "Appendix") that the relative variation of $\ell(x)$ is equal to the relative variation of $V_B(x)$, i.e.,

$$\ell'(x) = \frac{V_B'(x)\ell(x)}{V_B(x)}, \tag{11}$$

where the prime denotes the derivative with respect to x. According to Cubaud and Ho (2004), the case of a bubbly flow is characterized by $0.75 < \alpha_L < 1$, in the regime of which the pressure gradient in the liquid phase $p'(x)$ can be expressed as the pressure gradient along the microchannel for a single liquid phase divided by the liquid fraction, i.e.,

$$p'(x) = -\frac{\gamma \mu J_L}{2d_h^2 \alpha_L(x)}, \tag{12}$$

where $J_L = Q_L/A_\Sigma$ is the liquid superficial velocity in the microchannel and $\gamma = 56.8$ for a square channel or $\gamma = 64$ for a circular channel (Bruus 2008). The superficial velocity can also be expressed as

$$J_A(x) = \frac{J_L}{\alpha_L(x)}. \tag{13}$$

The pressure in the gas phase, denoted $p_G(x)$, can be calculated from the pressure in the liquid phase using the Young–Laplace equation:

$$p_G(x) = p(x) + \frac{4\sigma}{d(x)}, \tag{14}$$

where σ is the surface tension of the bubble–liquid interface.

A mass balance for the transferred species between the gas and the liquid phases, written for a control segment of the microchannel of length Δx, leads, for $\Delta x \to 0$, to the equation for the evolution along the microchannel of the concentration $C(x)$ of the dissolved gas into the liquid phase,

$$C'(x) = \frac{-\alpha_L(x)p_G'(x) + \alpha_L'(x)p_G(x) + \alpha_L^2(x)p_G'(x)}{\alpha_L^2(x)RT}, \tag{15}$$

with T the temperature (assumed constant along the microchannel) and R the ideal gas constant. Details for obtaining Eq. 15 are provided in "Concentration of the dissolved gas in the liquid phase along the microchannel" section of "Appendix."

Change in diameter for a bubble dissolving along the microchannel into a nonvolatile liquid has two origins: the mass transfer between the bubble and the liquid phase and the dependence of the bubble volume with the pressure.

Table 3 Input parameters of the dissolution model for CO_2 bubbles in water. The type of microchannel is specified when necessary

Parameter	Value
Q_L (μl min^{-1})	120
d_0 (μm)	140
d_h (μm)	200
A_Σ (m^2)	4×10^{-8} (square)
	$\pi \times 10^{-8}$ (circular)
D (m^2 s^{-1})	1.91×10^{-9}
ρ (kg m^{-3})	1000
μ (Pa s)	0.001
σ (N m^{-1})	0.0723
H (mol m^{-3} Pa^{-1})	0.000336
T (K)	298.15
ℓ_0 (mm)	5
p_0 (bar)	4
C_0 (mol m^{-3})	127
L_{out} (m)	0.8
γ	56.8 (square)
	64 (circular)

Performing a mass balance for a single bubble on a short time interval, and using the law of perfect gas, the equation for the evolution along the microchannel of the bubble diameter is

$$\frac{p'_G(x)d(x) + 3p_G(x)d'(x)}{6RT} = -\frac{1}{V_B(x)}k_l(x)[C_{\text{sat}}(x) - C(x)], \qquad (16)$$

where $C_{\text{sat}}(x) = H\,p_G(x)$ is the saturation concentration of the dissolved gas in the liquid, with H the Henry coefficient of the gas–liquid combination, and $k_l(x) = D\frac{\text{Sh}(x)}{d(x)}$ is the mass transfer coefficient between the bubble and the liquid. The details for obtaining Eq. 16 are provided in "Bubble diameter along a microchannel" of "Appendix."

To summarize, the dissolution model consists of 9 equations:

- four first-order ordinary differential equations (Eqs. 11, 12, 15 and 16);
- the Young–Laplace equation (Eq. 14);
- the equations for $\alpha_L(x)$ (Eq. 10) and for $J_A(x)$ (Eq. 13);
- the appropriate correlations to express $\text{Sh}(x)$ and $V_B(x)/J_A(x)$ as functions of $d(x)/d_h, \mu/(\rho D)$ and $\rho V_B(x)d(x)/\mu$ (see Tables 1, 2). The correlations to be used depend on the types of microchannel and interfacial boundary condition.

The four first-order ordinary differential equations need to be completed by four boundary conditions: $\ell(0) = \ell_0, d(0) = d_0, C(0) = C_0$ and $p(0) = p_0$. Alternatively, if the total length of the microchannel, say L_{out}, is known, the last boundary condition can be replaced by $p(L_{\text{out}}) = p_{\text{out}}$, where p_{out} is the pressure at the microchannel outlet.

Input parameters of the dissolution model are $\rho, \mu, \sigma, D, H, d_h, A_\Sigma, \gamma, L_{\text{out}}, T, Q_L, p_0, \ell_0, d_0, C_0$. The values of the physicochemical properties ρ, μ, σ, D and H depend on the liquid–gas combination used in the microchannel and on the temperature. The values of d_h, A_Σ, γ and L_{out} depend on the geometry of the microchannel, while T, Q_L, p_0 and C_0 are usual control parameters. The values of ℓ_0 and d_0 depend on the geometry of the bubbles generation system (T-junction, flow-focusing, co-flow, ...), as well as the control parameters of the model and the physicochemical properties of the liquid–gas combination. The nine output variables of the dissolution model are $p(x), p_G(x), d(x), C(x), \ell(x), V_B(x), \alpha_L(x), J_A(x)$ and $k_l(x)$.

The equations of the dissolution model are solved using Wolfram Mathematica 9.

3 Model capabilities

3.1 Influence of the interfacial boundary condition on gas dissolution

The dissolution of spherical CO_2 bubbles in water along a square microchannel is analyzed using the dissolution model. Bubbles with a stress-free interface or bubbles with a rigid interface are considered, in otherwise identical conditions. Input parameters of the dissolution model are given in Table 3, and the results are presented, in dimensionless forms, in Fig. 2 (left and center). It is worth mentioning that, using the values given in Table 3, $C_{\text{sat}}(0) = Hp_0 = 134\,\text{mol m}^{-3}$. As C_0 is taken equal to 127 mol m^{-3}, it means that, at $x = 0$, the liquid is, on purpose, not far from being saturated with CO_2. This initial condition enables highlighting qualitative differences between the different cases considered in this section, as well as in the following one.

As shown in Fig. 2, the pressure in the liquid phase is decreasing along the microchannel, as expected. The pressure in the gas phase is almost the same as in the liquid phase, but when the bubbles disappear (i.e., for $d \to 0$), the pressure in the gas phase becomes significantly larger than in the liquid phase due to the Laplace pressure [see Fig. 2 (center)]. The evolution of the pressure in the gas phase along the microchannel determines the evolution, along the microchannel, of the saturation concentration since $C_{\text{sat}}(x) = H\,p_G(x)$. It is worth mentioning that the slope of $p(x)$ is not constant because $\alpha_L(x)$ is not constant along the microchannel (see Eq. 12). This nonlinearity is however small and barely visible in Fig. 2. It can also be observed in Fig. 2 that the separation distance between

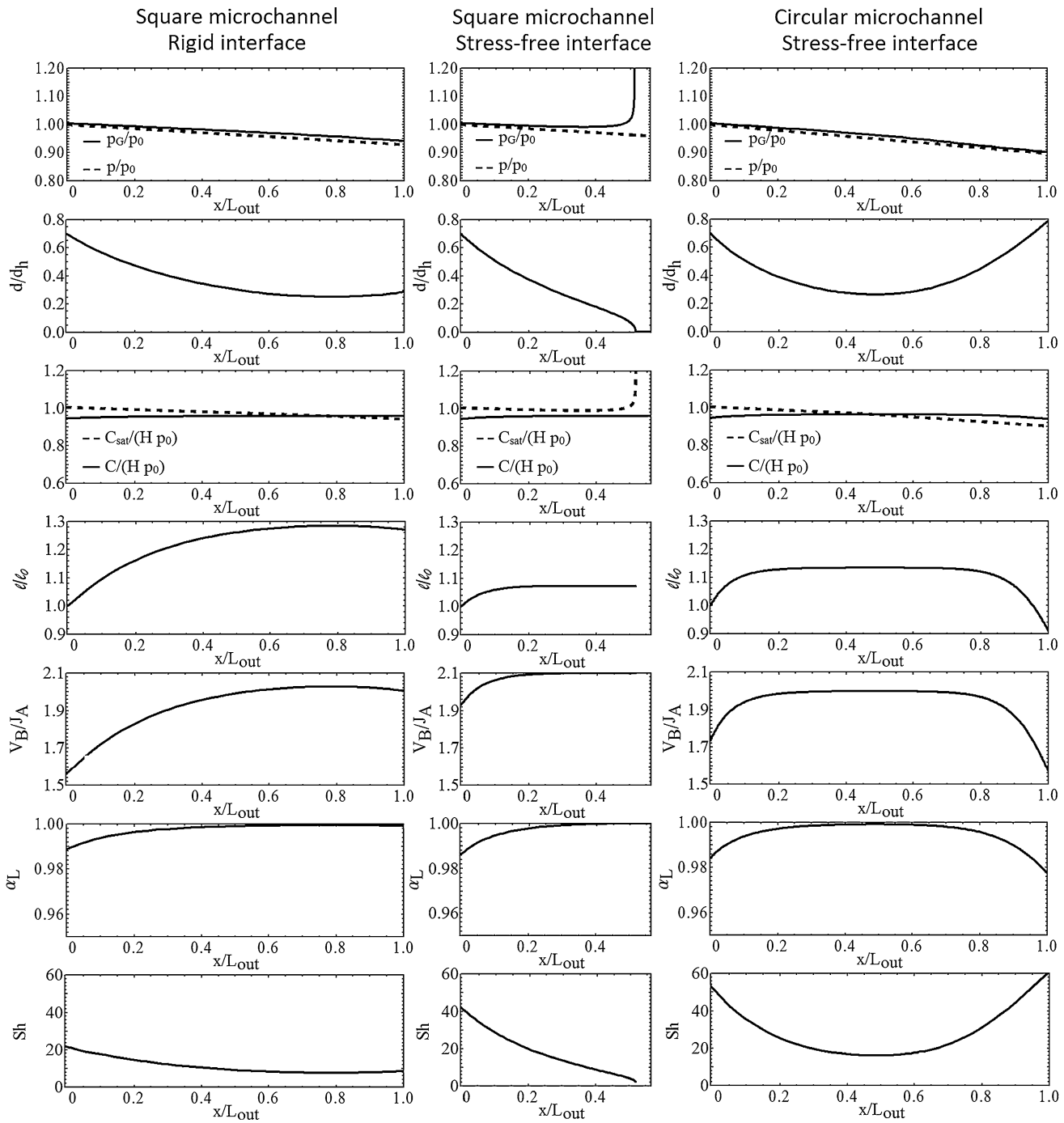

Fig. 2 CO_2 bubbles dissolving in water along a microchannel. Solutions of the dissolution model for: (*left*) a square microchannel containing bubbles with a rigid interface, (*center*) a square microchannel containing bubbles with a stress-free interface and (*right*) a circular microchannel containing bubbles with a stress-free interface, in otherwise similar conditions. Input parameters used to generate these plots are given in Table 3. Output variables, namely $p(x), p_G(x), d(x), C(x), C_{\text{sat}}(x), \ell(x), V_B(x), \alpha_L(x)$ and $k_l(x)$, are presented in dimensionless forms

the center of two successive bubbles, i.e., $\ell(x)$, does not vary much along the whole microchannel.

The evolution of $d(x)$ along the microchannel is due to two distinct phenomena. The pressure decrease along the microchannel tends to increase the bubble volume. The gas–liquid mass transfer tends to decrease the bubble volume when $C(x) < C_{\text{sat}}(x)$ (absorption) and tends to increase the bubble volume when $C(x) > C_{\text{sat}}(x)$ (desorption). As $p(x)$ is decreasing when x increases, a transition from absorption to desorption might occur in the microchannel,

especially at low values of k_l and when C_0 is close to $C_{\text{sat}}(0)$. If such a transition is encountered, a complete dissolution of the bubbles would not be obtained. Comparing the two first columns in Fig. 2, a complete dissolution is obtained in the case of a stress-free interface, while a partial dissolution is obtained in the case of a rigid interface.

At given values of $d(x)/d_h$ and $J_A(x)$, the bubble velocity $V_B(x)$ is higher for a bubble with a stress-free interface than for a bubble with a rigid interface (see Eqs. 1 and 5), as it is observed in Fig. 2 (left and center). Therefore, in a microchannel, a bubble with a stress-free interface reaches faster low values of $p_G(x)$, and thus low values of $C_{\text{sat}}(x)$, than a bubble with a rigid interface, in otherwise identical conditions. The time-averaged driving force for gas–liquid mass transfer is thus lower for the bubble with a stress-free interface than for the bubble with a rigid interface. On the other hand, at given values of $d(x)/d_h, \mu/(\rho D)$ and $\rho V_B(x)d(x)/\mu, k_l(x)$ is higher for a bubble with a stress-free interface than for a rigid interface (see Eqs. 2 and 6), as it is observed in Fig. 2 (left and center). For the cases presented in Fig. 2 (left and center), a complete dissolution is observed when a stress-free interface is considered, while a partial dissolution is observed when a rigid interface is considered. These observations imply that, for the conditions given in Table 3, the increase in $k_l(x)$ overcomes the decrease in the time-averaged driving force for the gas–liquid mass transfer, when a stress-free interface is considered instead of a rigid interface.

The boundary condition at the bubble–liquid interface is therefore of primary importance and can be linked in practice to the possible rigidity of the interface conferred by the presence of surfactants: A stress-free condition can be applied in the case of a clean interface, and a no-slip condition can be applied in the case of an interface "rigidified" under the flow by the presence of surfactants (see Sect. 1). Therefore, by changing from a clean interface to a "rigidified" interface, it is possible under certain conditions to switch between a complete and a partial dissolution of bubbles in microchannel. Similar conclusions have been observed in a circular microchannel instead of a square one and are thus not represented here.

3.2 Influence of the microchannel type on gas dissolution

In this section, the dissolution in water of spherical CO_2 bubbles with a stress-free interface is analyzed using the dissolution model. A circular or a square microchannel is considered, in otherwise similar conditions, as given in Table 3. Comparing the two last columns in Fig. 2 shows that a complete dissolution is obtained in the case of a square microchannel, while a partial dissolution is obtained in the case of a circular microchannel.

On the one hand, the bubble velocity $V_B(x)$ is smaller in the square than in the circular microchannel, even though it is not visible in Fig. 2. Indeed, $V_B(x)/J_A(x)$ appears to be smaller in the circular than in the square microchannel (see Fig. 2, center and right), but this apparent discrepancy is due to the fact that, for a fixed value of d_h, the cross-sectional area A_Σ is $4/\pi$ times larger for a square than for a circular microchannel (see Table 3). Therefore, at a given value of Q_L, all other parameters remaining the same, J_L and thus $J_A(x)$ are smaller in the square than in the circular microchannel, such that $V_B(x)$ is actually smaller in the square than in the circular microchannel. As a consequence, the time-averaged driving force for gas–liquid mass transfer is larger for bubbles in the square than in the circular microchannel, following the same reasoning than in the previous section. This behavior is reinforced by the fact that $-p'(x)$ is larger in the circular microchannel than in the square one (see Eq. 12), due to the larger values of γ and J_L in the circular microchannel.

On the other hand, $\text{Sh}(x)$ is larger in the circular microchannel than in the square one (see Fig. 2, center and right), which is due to the larger values of $\text{Re} = \rho V_B(x)d(x)/\mu$ in the circular microchannel than in the square one.

As a complete dissolution is observed in the square microchannel and not in the circular one, this indicates that, for the conditions given in Table 3, the increase in the time-averaged driving force for the gas–liquid mass transfer overcomes the decrease in $k_l(x)$, when a square microchannel is considered instead of a circular one. Similar conclusions have been observed when the interface is rigid instead of stress-free and are thus not represented here.

3.3 Parametric sensitivity analysis

The parametric sensitivity analysis presented here consists in monitoring the variation of the length needed for the complete dissolution of the bubbles, denoted L_{diss}, when the value of one input parameter is changed, the values of the other ones being kept constant, say at their reference values. The reference values used for the input parameters are the ones given in Table 3, except C_0 that is set to zero. Bubbles with a stress-free interface in a square microchannel are considered. The values of the different input parameters are varied such that d/d_h, Re and Sc remain in their ranges of validity of the correlations given in Table 1. Note that L_{diss} is independent on the density ρ: It cancels out in the correlations of Table 1 to calculate Sh since the exponents of Re and Sc are identical. Note that μ also cancels out in the correlations of Table 1 to calculate Sh, but it also appears in Eq. (12) of the model. Results of this parametric sensitivity analysis are given in Figs. 3 and 4.

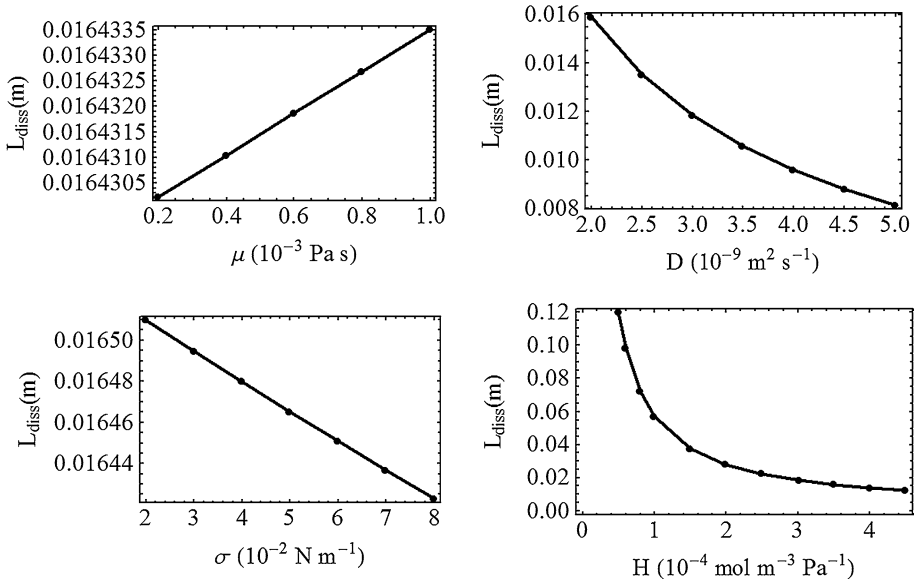

Fig. 3 Influence of the physicochemical properties on the complete dissolution length L_{diss} in a square microchannel with a stress-free interface

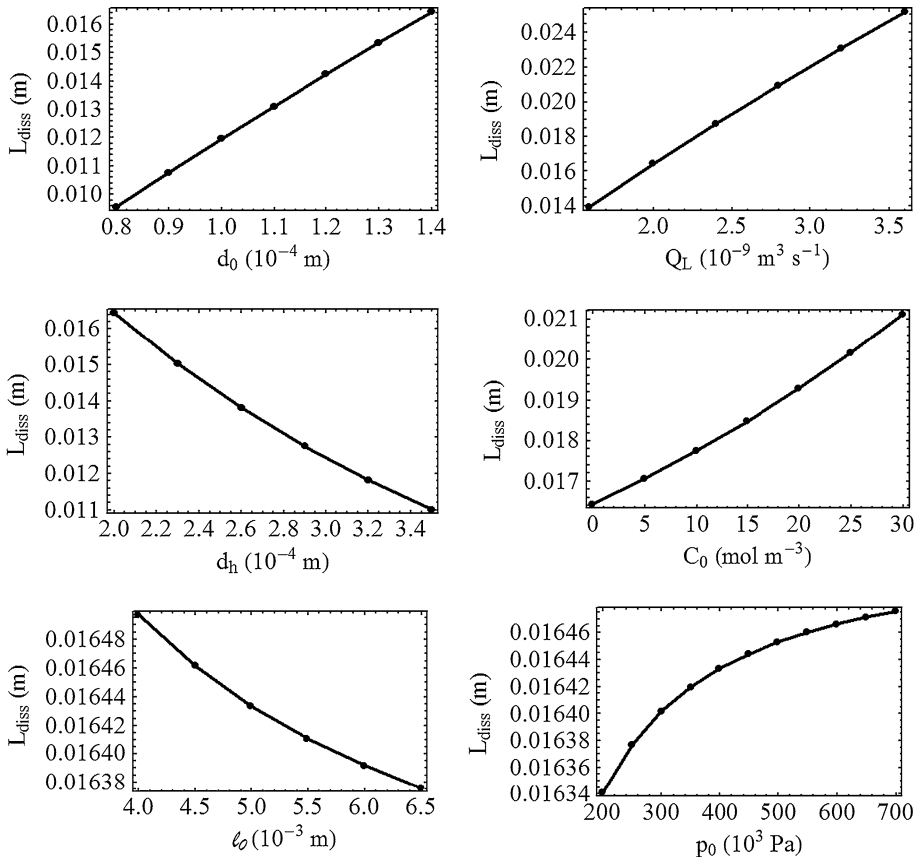

Fig. 4 Influence of the operating conditions on the complete dissolution length L_{diss} in a square microchannel with a stress-free interface

Trends presented in Fig. 3 can be understood as follows. As μ increases, the pressure drop in the liquid phase along the microchannel increases (see Eq. 12), leading to a larger decrease in $p(x), p_G(x)$ and thus $C_{sat}(x)$ along the microchannel. Therefore, the driving force for gas dissolution decreases and L_{diss} increases. The influence of μ on L_{diss} is however limited, because, as shown later, the influence of $p(x)$ or $p_G(x)$ on L_{diss} is small. When D increases, L_{diss} decreases because gas dissolution is promoted. When σ increases, L_{diss} decreases because $p_G(x)$ and thus $C_{sat}(x)$ increases. Nevertheless, the influence of σ on L_{diss} is small. Finally, an increase in H logically promotes the mass transfer

from the bubbles into the liquid phase and leads to a decrease in L_{diss}, which is clearly the most significant influence.

Trends presented in Fig. 4 can be understood as follows. When the initial size of the generated bubbles, d_0, increases, the microchannel length needed to dissolve them increases too. When Q_L and thus J_L increase, V_B increases (see Table 1 and Eqs. 9 and 13), leading to an increase in L_{diss}, as explained in Sect. 3.1. When d_h increases, J_L decreases for a constant Q_L and therefore L_{diss} decreases. When C_0 increases, the driving force for gas dissolution decreases and L_{diss} increases. When ℓ_0 increases, the distance between two successive bubbles increases. Therefore, the concentration in the liquid phase of the dissolved gas is lowered and gas dissolution is promoted. In Eq. 16, it can be seen that when p_G increases, the driving force for the dissolution of the bubbles increases but the amount of gas molecules in the bubbles increases too. These two increases have opposite effects on the change in L_{diss}. As the pressure gradient in the liquid phase is small (see Fig. 2) and as $C_0 = 0$, the dominating quantities in Eq. 16 are $p_G(x)d'(x)$ on the left-hand side and $C_{\text{sat}}(x) = H\,p_G(x)$ on the right-hand side, such that $p_G(x)$ can roughly be simplified in this equation. It explains the small influence of $p_G(x)$, and thus of $p(x)$ and p_0, on L_{diss}.

Influences of d_0 and ℓ_0 on L_{diss} have been analyzed here by considering them as independent of p_0 and Q_L. But, as mentioned at the end of Sect. 2, ℓ_0 and d_0 should be related to p_0 and Q_L, depending, among others, on the bubbles generation system in use (T-junction, flow-focusing, co-flow).

It is important to emphasize that this parametric sensitivity analysis is only an example, to give general trends. The amplitude of the variation of L_{diss} with the variation of a given input parameter might differ if different reference values are used. Using the dissolution model, correlations between L_{diss} and the input parameters might be constructed. However, given the large number of independent parameters and the fact that the model by itself is relatively easy to solve, we recommend to simply calculate the solutions for a specific set of parameters when necessary.

3.4 Comparison to the literature

Experimental data obtained by Cubaud et al. (2012) can be compared to results obtained with the dissolution model. Indeed, in their work, a bubbly flow was observed during their experiments of CO_2 bubbles dissolution in water, in a nearly square microchannel. The microchannel had a width $w_C = 87\,\mu\text{m}$, a height $h_C = 100\,\mu\text{m}$ and a length $L_C \approx 10\,\text{cm}$.

In the experiments of Cubaud et al. (2012), V_B, d, ℓ and the bubble traveling time t were recorded along the microchannel, for various operating conditions. As defined previously, α_L and J_A can be calculated from these measurements as follows:

$$\alpha_L = \frac{Q_L}{Q_L + \frac{\pi d^3}{6}\frac{V_B}{\ell}} \quad \text{and} \quad J_A = \frac{Q_L}{\alpha_L w_C h_C},$$

where Q_L is the liquid volumetric flow rate in the microchannel.

For a given experimental set of Cubaud et al. (2012), the part of the experimental data corresponding to a bubbly flow regime can be compared to the results of the dissolution model, with $d_h = \frac{2w_C h_C}{w_C + h_C}$. To use the model, the values of d_0, ℓ_0, C_0 and p_0 are taken at the position of the microchannel where the condition $d_0 = 0.75\,d_h$ is reached in the experiment. While ℓ_0 is directly given by Cubaud et al. (2012), C_0 is evaluated by a mass balance using the recorded experimental data. The pressure p_0, also needed to evaluated C_0, is adjusted such that the simulated pressure at the end of the microchannel is equal to the atmospheric pressure.

In Fig. 5, the dissolution model is compared with two sets of experimental data by Cubaud et al. (2012). For each of them, the dissolution model has been computed with either a stress-free or a rigid bubble–liquid interface. When a stress-free interface is considered, Eqs. 1 and 2 are used and it is referred to hereafter as the "stress-free model." When a rigid interface is considered, Eqs. 5 and 6 are used and it is referred to hereafter as the "rigid interface model."

As it can be seen in Fig. 5, for V_B/J_A, the solutions of the stress-free interface model overestimate the experimental results and the solutions of the rigid interface model underestimate them. This observation suggests that the liquid phase used in the experiments of Cubaud et al. (2012) could have been contaminated, which would invalidate both the stress-free and the no-slip conditions on the bubble surface and lead to values of V_B/J_A between the two limiting values obtained considering these boundary conditions. The bubble velocity V_B is lower in the case of a bubble with a rigid interface than in the case of a bubble with a stress-free interface because the adsorption of surfactants on the bubble–liquid interface "rigidifies" it under the flow, which thus increases the friction and slows down the bubble. Nevertheless, the agreement is still good between the computed and the experimental data for d/d_h and α_L. For d/d_h, the experimental results are almost in between the values of d/d_h computed using the stress-free and the rigid interface models. The values of d/d_h computed with a rigid interface are higher than those computed with a stress-free interface because the dissolution of a bubble is faster in the latter case, as explained in Sect. 3.1.

It is important to note that, in our previous work (Mikaelian et al. 2015), the correlations presented in Table 1 were constructed as being ℓ-independent; i.e., the values of ℓ used in the computations were large enough such that the computed Sh were independent of ℓ. This condition might lead to a discrepancy between the dissolution model and

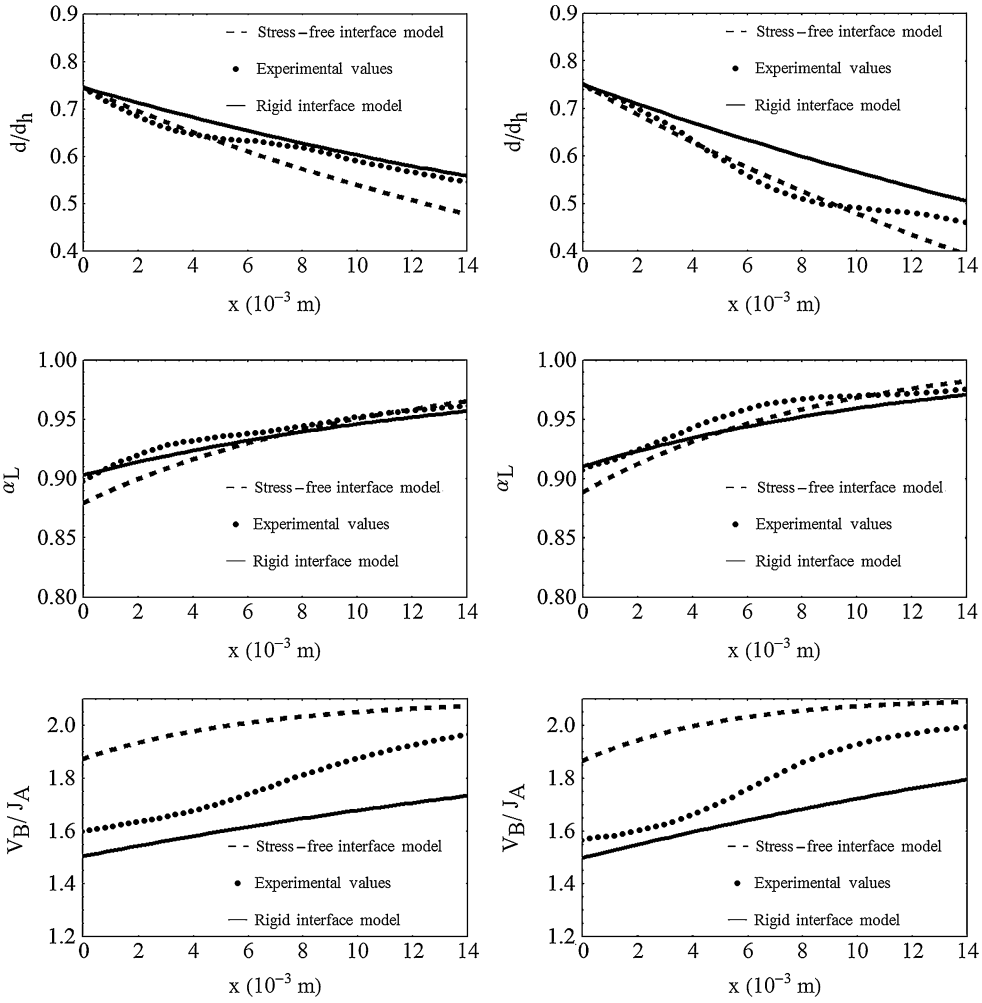

Fig. 5 Comparison between the values of $d/d_h, \alpha_L$ and V_B/J_A computed with the stress-free interface model and with the rigid interface model, and the experimental results of Cubaud et al. (2012) for $Q_L = 110\,\mu\text{l}\,\text{min}^{-1}$ (*left*) and $Q_L = 120\,\mu\text{l}\,\text{min}^{-1}$ (*right*)

the experimental results of Cubaud, as the values of ℓ met in these experiments are smaller than the ones considered in our previous work in order to build the correlations of Table 1.

It is also worth mentioning that to establish the comparison presented in Fig. 5, it is assumed that the correlations obtained in Table 1 for a square microchannel are still valid for a rectangular microchannel, provided its aspect ratio remains close to unity as it is the case here since $w_C/h_C = 0.87$.

To provide another link with data available in the literature, it is interesting to compare the mass transfer between the gas and liquid phases in microchannels with a bubbly flow regime and with a slug flow regime, which is the most widely used regime. In Yue et al. (2007), k_l was evaluated in the slug flow regime for CO_2 bubbles moving in water along a rectangular microchannel with a hydraulic diameter of 667 μm. For a superficial velocity of the liquid $J_L = Q_L/A_\Sigma$ equals to 0.2 m s^{-1} and a superficial velocity of the gas $J_G = Q_G/A_\Sigma$ equals to 1 m s^{-1}, $k_l \approx 80 \times 10^{-5}$ m s^{-1} was measured experimentally by Yue et al. (2007). For a square microchannel with the same hydraulic diameter and the same J_L, a bubbly flow can be observed for J_G equal to 0.03 m s^{-1} (see Cubaud and Ho 2004). If we consider CO_2 bubbles separated by a distance of 5 mm moving in water in this microchannel and for these J_L and J_G, Eqs. 1 and 2 with $k_l = \frac{ShD}{d}$ allow evaluating k_l for $0.15 < d/d_h < 0.75$ and lead to 28×10^{-5} m $s^{-1} < k_l < 42 \times 10^{-5}$ m s^{-1}. The value of k_l in the bubbly flow regime is thus of the same order of magnitude than in the slug flow regime, though quantitatively lower in this specific example. While the flow recirculation in the liquid slugs between two successive bubbles is known to enhance the mass transfer (Kashid et al. 2011), we have shown in Mikaelian et al. (2015) that liquid recirculation also exists between spherical bubbles under certain conditions, which could thus explain the comparable k_l obtained in slug and bubbly flow regimes.

4 Model applications and validity

The dissolution model can be used in the bubbly flow regime and in the ranges of applicability of the correlations given in Table 1, for different purposes like:

- the evaluation of the length of a microchannel necessary for a complete dissolution of spherical bubbles of a given gas in a given nonvolatile liquid;
- the evaluation of the maximum concentration of a dissolved gas in the liquid phase and the position along the microchannel where this maximum is reached, in the case of partial dissolution;
- the optimization of the bubble dissolution with a stress-free or a rigid interface along a square or a circular microchannel.

The correlations proposed to calculate V_B/J_A and Sh (Eqs. 1–8) have been established in the ranges $0.15 \leq d/d_h \leq 0.75, 1.70 \leq \mathrm{Re} \leq 39.84$ and $152 \leq \mathrm{Sc} \leq 551.3$. Therefore, when the dissolution model is used to simulate the complete dissolution of bubbles, these correlations are used beyond their domain of strict validity. Nevertheless, when $d \to 0, V_B/J_A \to 2.1$ is expected for a square microchannel and $V_B/J_A \to 2$ is expected for a circular microchannel. Indeed, these values are the theoretical ratios between the maximum and the mean velocities of a laminar one-phase flow in a square and a circular microchannel, respectively (Bruus 2008). These limits are coherent with the equations proposed in Table 1 regarding V_B/J_A. Moreover, as the correlations given in Table 1 regarding Sh have been constructed such that $\mathrm{Sh} \to 2$ as $d \to 0$ or $\mathrm{Re} \to 0$, which corresponds to the pure diffusion limit, we expect these correlations to be also accurate by interpolation for $0 \leq d/d_h < 0.15$.

It is worth emphasizing that the dissolution model and the correlations given in Table 1 proposed here can be used for gas absorption in a liquid, but also for gas desorption along a microchannel, provided a chain of spherical bubbles is already present.

Most often, the gas phase in a gas–liquid two-phase flow is not pure. The extension of our dissolution model for a gas phase containing several components is however straightforward. Indeed, one simply has to duplicate Eqs. 15 and 16 for the concentration of each component, replace the gas pressure by the corresponding partial pressure and use the appropriate Henry coefficient for each component, as well as the corresponding diffusion coefficient in the definition of $k_l(x)$; Eqs. 12 and 14 remain identical; i.e., they still involve the total pressure. The initial concentrations and partial pressures should also be given for each component. An interesting situation to be studied with such a multi-component model would be the competition between the absorption of one component, from bubble to liquid, with the desorption of another component, from liquid to bubble. We can think, for instance, of the dissolution of CO_2 bubbles into water that already contains dissolved air.

In this work, the liquid has been assumed to be nonvolatile. If this is not the case, the liquid would evaporate into the newly generated gas bubbles, which would influence their dissolution. The resulting vapor would coexist with the gas and the multi-component model mentioned in the previous paragraph should apply, provided the right-hand side of Eq. 16 written for the vapor component is modified accordingly.

Colloid-armored bubbles have been obtained in microchannels by Park et al. (2009): Bubbles are formed at a T-junction in a flow of colloidal suspension, and as the gas dissolved into the liquid, the density of colloids adsorbed at the bubble–liquid interface increases, which tends to "rigidify" the interface. This system could then be sought as the limiting case of our dissolution model with rigid bubble–liquid interface and could thus be used for validating our model in that case. However, the exchange area varies also with the particle density, which would require modifying the present model. Apart from that point, and as the surface density of particles overcomes the close packing limit, the interface could buckle, either because the interface is still permeable to gas or because the pressure is suddenly increased. Nevertheless, as far as bubbles with buckled surfaces are concerned, it would definitely modify the hydrodynamics around the bubbles, hence the flow structure and the mass transfer. Similar conclusions have been obtained by Terwagne et al. (2014) who showed how the aerodynamics around spheres is strongly affected by the presence of buckling at their surfaces, as for a golf ball. Consequently, the correlations given in Table 1 would not be valid anymore and new correlations should be obtained first and then incorporated in the present dissolution model.

Finally, the correlations used in our dissolution model are based on the hypothesis that the bubbles travel along the centerline of the microchannel, which is questionable because of the buoyancy effect that is hardly negligible given the high-density contrast between the gas and the liquid. Nevertheless, Stan et al. (2011) have shown that bubbles, despite their buoyancy, can flow without touching the top wall of a channel because hydrodynamic lift forces balance their buoyant forces. The vertical position of bubbles depends on their size and buoyancy, as well as on the viscosity and velocity of the carrier liquid. For a density contrast of about 1000 kg/m^3 and $d/d_h = 0.67$, the authors even showed that the bubbles remain on the centerline for $\mu J_A \geq 5 \times 10^{-4}$ Pa m. Now, typical values of μJ_A considered in this paper (see Table 3), and in the experiment of Cubaud et al. (2012), are one order of magnitude smaller. Buoyancy should thus displace the bubble off-center, the exact position of which depends on $d/d_h, \rho, \mu$ and J_A. Therefore, and as concluded in Mikaelian et al. (2015), appropriate correlations for the bubble velocity and the Sherwood number should be first obtained in the case of off-center buoyant bubbles and then incorporated in the present dissolution model. Alternatively, future experiments specifically designed for validating our present

dissolution model could use a much viscous carrier fluid than water, such that lift forces are large enough to maintain the bubbles at the center of the microchannel, as described in Stan et al. (2011).

5 Conclusions and perspectives

In this paper, the correlations established by Mikaelian et al. (2015) and presented in Table 1 are integrated into a mathematical model of a whole microchannel, where a chain of spherical bubbles is dissolving into a nonvolatile liquid. This dissolution model is based on mass and momentum balances. Pure gas bubbles are considered in this model, with either a stress-free or a rigid interface, in a square or a circular microchannel. This model enables predicting, in these different cases, the evolution of the bubble diameter, the bubble velocity, the separation distance between two successive bubbles, the liquid fraction, the pressure in both the liquid and the gas phases, the concentration of the dissolved gas in the liquid phase and the mass transfer coefficient between the bubble and the liquid phase. The use of the dissolution model shows the influence, on the gas dissolution rate, of the interfacial boundary condition and of the microchannel type. The three cases considered in Sects. 3.1 and 3.2 and presented in Fig. 2 highlight the complexity of the interactions between the different factors influencing the transport phenomena taking place within a microchannel where a bubbly flow regime is encountered. A parametric sensitivity analysis of the dissolution model is also carried out to highlight the influence of the input parameters on the length of the microchannel necessary for complete dissolution (L_{diss}).

A good agreement relying on a relative difference of less than 20 percent is observed between data predicted by the dissolution model and experimental data of Cubaud et al. (2012), for a nearly square microchannel. This conclusive comparison can be seen as a first validation of the dissolution model as well as of the correlations for V_B/J_A and Sh proposed by Mikaelian et al. (2015). The fact that the experimental data for V_B/J_A lie between the two limits of a stress-free and a rigid interfacial boundary condition indicates a possible contamination of the interface that may be responsible for conferring a partially rigid behavior to the bubble surface in the experiments. Another possible explanation for the discrepancy between experiment and theory is the possible role of buoyancy as discussed in Sect. 4. Further investigations are needed to verify these conjectures.

Additionally, as only the transition from a slug flow to a bubbly was characterized by Cubaud et al. (2012), it could be interesting to set up an experiment where only a bubbly flow is observed along an entire microchannel. The results could then enable a more profound validation of the dissolution model proposed in this work.

The comparison between values of k_l in the bubbly flow regime estimated using the correlations given in Table 1 and values of k_l evaluated experimentally in the slug flow regime by Yue et al. (2007) shows that they are of the same order of magnitude. One possible explanation is that, like in the slug flow regime, flow recirculations between two successive bubbles can be present in the bubbly flow regime, as showed in Mikaelian et al. (2015).

The proposed correlations and model for the dissolution of a chain of spherical bubbles can be applied for square and circular microchannels of various sizes and for various combinations of gas and liquid. Therefore, they can be used, for instance, for designing lab-on-a-chip devices for the absorption of various gases in various liquids. Contrarily, they can also be used for computing bubble desorption and growth along a microchannel.

Finally, we believe that the two-step methodology we have developed here, which consists in first establishing correlations numerically (see Mikaelian et al. 2015), and second incorporating them in a dissolution model that relies on balance equations, should pave the way for modeling the dissolution of a chain of liquid droplets into another miscible carrying liquid in microchannels, as encountered, for instance, in all-aqueous droplet microfluidics (Ziemecka et al. 2011a, b), in microfluidic protein encapsulation (see, e.g., Trana et al. 2011) or in microfluidic fabrication of polymersomes (see, e.g., Thiele et al. 2010).

Acknowledgments The authors thank Sam Dehaeck for the useful comment about the possible volatility of the liquid. D.M. and B.S. acknowledge the Fonds de la Recherche Scientifique (F.R.S.-F.N.R.S.) for their financial contribution. This research has been performed under the umbrella of the COST action MP1106 and also takes part in the Inter-university Attraction Pole Programme (IAP 7/38 MicroMAST) initiated by the Belgian Science Policy Office.

Appendix: Supplementary materials for the model construction

Separation distance between two successive bubbles along the microchannel

For $\Delta x \to 0$, it can be considered that a bubble moves from x to $x + \Delta x$ at a velocity $V_B(x)$. The time for this bubble to travel the distance Δx is equal to $\Delta x / V_B(x)$. During this time, the preceding bubble moves on a distance $\Delta x - \ell(x + \Delta x) + \ell(x)$ at a velocity $V_B(x - \ell(x))$:

$$\frac{\Delta x}{V_B(x)} = \frac{\Delta x - \ell(x + \Delta x) + \ell(x)}{V_B(x - \ell(x))}, \tag{17}$$

or, after rearrangement,

$$\frac{\ell(x + \Delta x) - \ell(x)}{\Delta x} = \frac{V_B(x) - V_B(x - \ell(x))}{V_B(x)}. \tag{18}$$

For $\Delta x \to 0$, Eq. 18 leads to:

$$\ell'(x) = \frac{V_B(x) - V_B(x - \ell(x))}{V_B(x)}, \tag{19}$$

where the prime denotes the derivative with respect to x. As $\ell(x) \ll x$, except of course in the vicinity of the inlet, $V_B(x) - V_B(x - \ell(x))$ is approximated by the first order of its Taylor expansion, i.e., $V_B'(x)\ell(x)$. Equation 19 then simplifies into Eq. 11.

Concentration of the dissolved gas in the liquid phase along the microchannel

For a control segment of the microchannel of length Δx (see Fig. 6), the following mass balance can be written for the transferred species between the gas phase and the liquid phase, using the ideal gas law:

$$Q_L C(x) + Q_G(x)\frac{p_G(x)}{RT} = Q_L C(x + \Delta x) + Q_G(x + \Delta x)\frac{p_G(x + \Delta x)}{RT}. \tag{20}$$

Q_L is taken independent of x thanks to the fact that the gas density is much lower than the liquid density, such that the amount of gas dissolved in the liquid does not significantly affect its flow rate.

Using Eq. 9, Eq. 20 can be rearranged as

$$C(x) + \frac{1 - \alpha_L(x)}{\alpha_L(x)}\frac{p_G(x)}{RT} = C(x + \Delta x) + \frac{1 - \alpha_L(x + \Delta x)}{\alpha_L(x + \Delta x)}\frac{p_G(x + \Delta x)}{RT}. \tag{21}$$

For $\Delta x \to 0$, Eq. 21 becomes

$$C'(x) = -\frac{1}{RT}\left(\frac{1 - \alpha_L(x)}{\alpha_L(x)} p_G(x)\right)', \tag{22}$$

or equivalently recasts into Eq. 15.

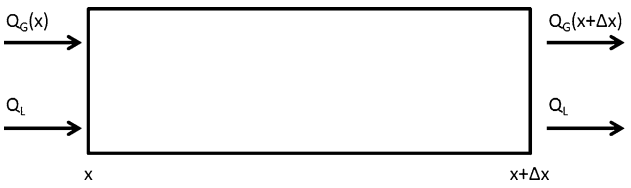

Fig. 6 Control segment of the microchannel of length Δx

Bubble diameter along the microchannel

If a bubble is at the coordinate x at time t and at the coordinate $x + \Delta x$ at time $t + \Delta t$ and if $\Delta t \to 0$ is considered, Δt can be replaced by $\Delta x / V_B(x)$ and the following mass balance can be written for the transferred species between the gas phase and the liquid phase, using the ideal gas law:

$$\frac{p_G(x + \Delta x)}{RT}\frac{\pi d^3(x + \Delta x)}{6} - \frac{p_G(x)}{RT}\frac{\pi d^3(x)}{6} = -\frac{\Delta x}{V_B(x)}\pi d(x)^2 k_l(x)[C_{\text{sat}}(x) - C(x)], \tag{23}$$

For $\Delta x \to 0$, Eq. 23 becomes

$$\frac{1}{6RT}\left(p_G(x)\, d^3(x)\right)' = -\frac{d^2(x) k_l(x)}{V_B(x)}[C_{\text{sat}}(x) - C(x)], \tag{24}$$

or equivalently recasts into Eq. 16.

References

Abolhasani M, Gunther A, Kumacheva E (2014) Microfluidic studies of carbon dioxide. Angew Chem Int Ed 53:2–13

Bruus H (2008) Theoretical microfluidics, vol 18. Oxford University Press, Oxford, pp 41–50, 75

Clift R, Grace JR, Weber ME (1978) Bubbles, drops and particles. Academic Press, New York

Cubaud T, Ho CM (2004) Transport of bubbles in square microchannels. Phys Fluids 16:4575

Cubaud T, Sauzade M, Sun R (2012) CO_2 dissolution in water using long serpentine microchannels. Biomicrofluidics 6:022002

Haberman WL, Morton RK (1953) An experimental investigation of the drag and shape of air bubbles rising in various liquids. David Taylor Model Basin, Report 802

Kashid MN, Renken A, Kiwi-Minsker L (2011) Gas–liquid and liquid–liquid mass transfer in microstructured reactors. Chem Eng Sci 66(17):3876–3897

Kim N, Evans ET, Park DS, Soper SA, Murphy MC, Nikitopoulos DE (2011) Gas–liquid two-phase flows in rectangular polymer micro-channels. Exp Fluids 51(2):373–393

Leitner W (2002) Supercritical carbon dioxide as a green reaction medium for catalysis. Acc Chem Res 35:746–756

Mikaelian D, Haut B, Scheid B (2015) Bubbly flow and gas–liquid mass transfer in square and circular microchannels for stress-free and rigid interfaces. CFD analysis. Microfluid Nanofluid. doi:10.1007/s10404-015-1578-0

Park JI, Nie Z, Kumachev A, Abdelrahman AI, Binks BP, Stone HA, Kumacheva E (2009) A microfluidic approach to chemically driven assembly of colloidal particles at gas–liquid interfaces. Angew Chem Int Ed 48:5300–5304

Shim S, Wan J, Hilgenfeldt S, Panchal PD, Stone HA (2014) Dissolution without disappearing: multicomponent gas exchange for CO_2 bubbles in a microfluidic channel. Lab Chip 14(14):2428–2436

Song H, Chen DL, Ismagilov RF (2006) Reactions in droplets in microfluidic channels. Angew Chem Int Ed 45(44):7336–7356

Stan CA, Guglielmini L, Ellerbee AK, Caviezel D, Stone HA, Whitesides GM (2011) Sheathless hydrodynamic positioning of buoyant drops and bubbles inside microchannels. Phys Rev E 84:036302

Sun R, Cubaud T (2011) Dissolution of carbon dioxide bubbles and microfluidic multiphase flows. Lab Chip 11:2924–2928

Terwagne D, Brojan M, Reis PM (2014) Smart morphable surfaces for aerodynamic drag control. Adv Mater 26:6608

Thiele J, Abate AR, Shum HC, Bachtler S, Frster S, Weitz DA (2010) Fabrication of polymersomes using double-emulsion templates in glass-coated stamped microfluidic devices. Small 6:1723–1727

Trana V-T, Benot J-P, Venier-Julienne M-C (2011) Why and how to prepare biodegradable, monodispersed, polymeric microparticles in the field of pharmacy? Int J Pharm 407:1–11

Triplett KA, Ghiaasiaan SM, Abdel-Khalik SI, Sadowski DL (1999a) Gas–liquid two-phase flow in microchannels, Part I: two-phase flow patterns. Int J Multiph Flow 25(3):377–394

Triplett KA, Ghiaasiaan SM, Abdel-Khalik SI, LeMouel A, McCord BN (1999b) Gas–liquid two-phase flow in microchannels, Part II: void fraction and pressure drop. Int J Multiph Flow 25(3):395–410

Voicu D, Abolhasani M, Choueiri R, Lestari G, Seiler C, Menard G, Greener J, Guenther A, Stephan DW, Kumacheva E (2014) Microfluidic studies of CO_2 sequestration by frustrated Lewis pairs. J Am Chem Soc 136:3875–3880

Yue J, Chen G, Yuan Q, Luo L, Gonthier Y (2007) Hydrodynamics and mass transfer characteristics in gas–liquid flow through a rectangular microchannel. Chem Eng Sci 62(7):2096–2108

Ziemecka I, van Steijn V, Koper GJM, Kreutzer MT, van Esch JH (2011a) All-aqueous core–shell droplets produced in a microfluidic device. Soft Matter 7:9878–9880

Ziemecka I, van Steijn V, Koper GJM, Rosso M, Brizard AM, van Esch JH, Kreutzer MT (2011b) Monodisperse hydrogel microspheres by forced droplet formation in aqueous two-phase systems. Lab Chip 11:620–624